

Out-of-plane polarimetric imaging of skin: Surface and subsurface effects

Jessica C. Ramella-Roman^{*a,b}, Don Duncan^a, Thomas A. Germer^b
^aApplied Physics Laboratory- Johns Hopkins University, Laurel, MD
^bNational Institute of Standards and Technology, Gaithersburg, MD

ABSTRACT

True borders of certain skin cancers are hard to detect by the human eye. For this reason, techniques such as polarized light imaging have been used to enhance skin cancer contrast before Mohs surgery procedures. In standard polarized light imaging the effect of the rough surface is minimized using a matched boundary, such as a glass slide and gel. Moreover, the surface glare is eliminated using skewed illumination. In this paper, we study the effect of the surface roughness on the polarized light backscattered from the skin. We demonstrate that rough surface effects can be minimized using out-of-plane polarized illumination in conjunction with¹ polarized viewing.

1. INTRODUCTION

Polarized light imaging has been used in dermatology to enhance the borders of certain skin lesions, such as basal cell carcinoma and squamous cell carcinoma^{1,2}. A typical set up for polarized light imaging is shown in Fig. 1. A camera views the skin perpendicular the surface. The source illuminates the skin obliquely about 20° from the surface normal. Incident light is linearly polarized, with its electric field oriented parallel (p) to the plane defined by the locations of the source, the illuminated tissue, and the camera. A glass plate, often with an index-matching gel or fluid, contacts the skin in the image plane to ensure a flat surface. Glare due to specular reflection off the air/glass interface and the glass/skin interface is deflected obliquely and misses the camera. Only light scattered from within the skin is imaged by the camera. Finally, a linear polarization analyzer is placed in front of the camera. Two images are acquired, the first image (pp) with the analyzer aligned parallel with the scattering plane, and the second image (ps) with the analyzer aligned perpendicular (s) to the scattering plane.

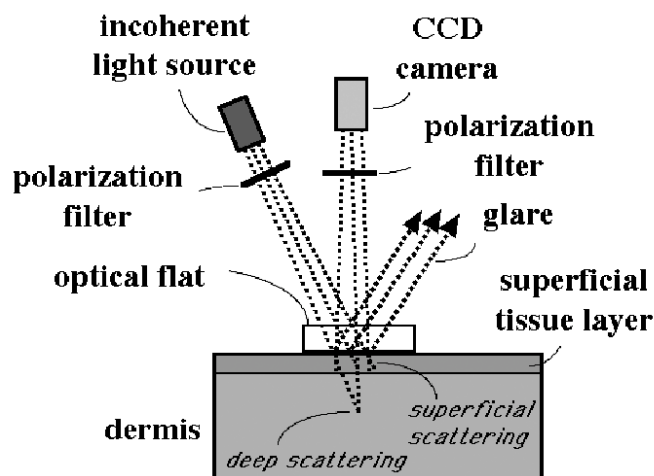


Figure 1 - Typical set up for polarized light imaging

¹ * jessica.ramella-roman@jhuapl.edu; phone 1 240 228-0595

Photons backscattered from superficial layers largely retain the polarization orientation of the source and contribute more strongly to the pp image. Light returning from deeper layers is multiply scattered, and these photons contribute equally to the ss and pp images. The polarized light image Pol is constructed from

$$Pol = \frac{pp - ps}{pp + ps} \quad (1)$$

By subtracting ps from pp , we eliminate the contribution of the multiply scattered photons. By normalizing by $pp + ps$, we cancel the variation in illumination and the effect of superficial melanin pigmentation.

The index-matching glass plate guarantees a flat boundary eliminating scattering from the exposed rough skin. Eliminating the glass boundary would be particularly advantageous in a clinical setting since it would eliminate physical contact with the patient. When in-plane illumination is used, as in Fig. 1, the light scattering from a rough surface also contributes to the polarized image. In such conditions, it was found that in-plane illumination from different angles could not eliminate the rough surface effect.

Germer *et al.*^{3,4} used light scattering ellipsometry to distinguish surface from subsurface scattering from a variety of materials, such as silicon wafers, glass, and metals. It was found that a number of different single-scattering mechanisms did not depolarize the light, but yielded different polarization states. They further found that contrast between the different mechanisms was greatest when light was incident with its electric field parallel to the plane of incidence, and when the scattered light was viewed out of that plane. We use an imaging setup that takes advantage of these findings to eliminate the influence of the light scattering from the rough surface, thus highlighting the subsurface scattered light. We show that when using this out-of-plane illumination technique the effect of the rough surface on the images pp and ps can be minimized by choosing an azimuth angle ϕ larger than 50° and a inclination angle $\theta = 45^\circ$ for the source and $\theta = -45^\circ$ for the detector.

2. MATERIALS AND METHODS

Two goniometric imaging set-ups were used to study in-plane and out-of-plane polarized light scattering from fresh porcine skin samples. The first experimental apparatus is shown in Fig. 2. In this system, a source arm rotates about a sample support, while the detector is at a fixed location normal to the sample. All elements lie in the same plane.

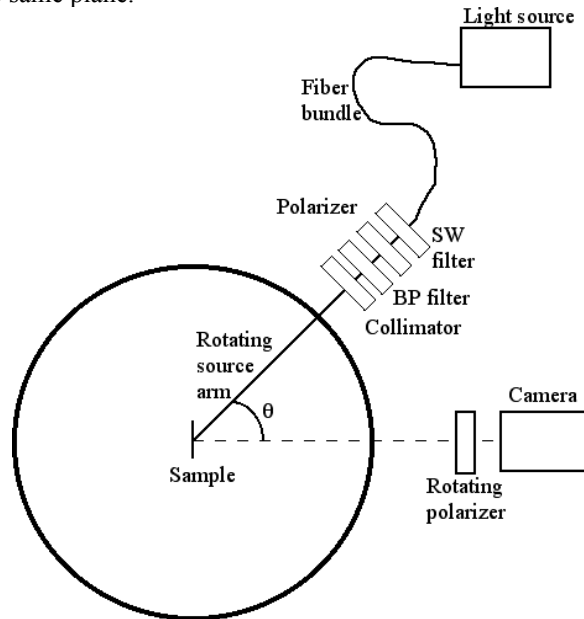


Figure 2- In plane polarized set-up

An incoherent light source (Oriel, Stratford, CT⁸) was coupled to a fiber bundle; the tip of the fiber bundle was connected to the rotating source-arm so that different incident angles could be achieved. Three

quasi-monochromatic wavelengths were sequentially chosen using band-pass filters (bandwidth 10 nm) centered respectively at 543 nm, 633 nm, and 694 nm (Newport Inc, Irvine CA). A short-wave pass filter was also used to eliminate infrared radiation. The incident beam was collimated, and the beam diameter was approximately 3 cm. The incident beam was polarized with a linear polarizer (Meadowlark, Frederick, CO) oriented parallel (p) to the camera-sample-source plane (reference plane). The source assembly was mounted on a motorized rotating arm (Newport Inc, Irvine CA) so that the source incident angle could be varied. The source arm moved by 5° increments from -70° to 70° , where 0° corresponds to illumination normal to the sample. The detector was a monochrome 10-bit 600×600 pixel digital camera (Lumenera, Ottawa, On, Canada) positioned normal to the sample. A polarizer was mounted on a motorized rotational stage in front of the camera in order to filter three different linear polarization states: (p) parallel, (s) perpendicular, and 45° to the reference plane. The distance from the sample to the camera was about 100 cm. The system was fully automated with Matlab software.

The samples were square samples of freshly excised porcine skin (4 cm^2) obtained from a local butcher. The skin samples were shaved and brushed clean. Dehydration of the skin samples was minimized by surrounding them with towels previously soaked in a saline solution. The samples were clamped to a support and positioned in front of the camera and at the pivotal point of the source arm. For every source angle three images were captured corresponding to the three p , s , and 45° analyzer positions. 210 images were collected.

The second goniometric system, shown in Fig. 3, uses out-of-plane illumination. In this set-up the source arm was oriented at an angle $\theta = 45^\circ$ with respect to the sample surface normal. The angle θ remained fixed at all times; the arm was allowed to move about an azimuth angle ϕ . The angle ϕ could rotate from 0° to 140° in steps of 2° .

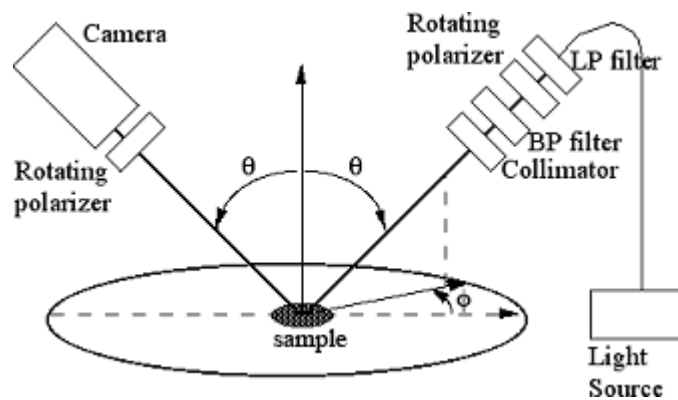


Figure 3- Out of plane polarized set-up

The source arm consisted of a short-pass filter to eliminate infrared radiation, followed by a linear polarizer on a computer-controlled rotation stage, followed by a band-pass filter centered on 543 nm (bandwidth 10 nm), and finally a lens to collimate the beam. The incident beam polarization was rotated into one of three different linear states parallel (p), perpendicular (s), and 45° with respect to the plane of incidence. The diameter of the incident beam was about 3 cm. The detector was fixed at the same angle θ as the source. A linear polarizer on a computer-controlled rotation stage to analyze three different linear states parallel (p), perpendicular (s), and 45° to the viewing plane (defined by the sample normal and the viewing direction). The detector was a monochrome 10-bit 600×600 pixel digital camera and lens assembly.

Two different materials were studied during out-of-plane experiments: an aluminum gold coated sample whose surface was roughened with electro-discharge machining, and porcine skin samples. The samples were also measured with a white light interferometric microscope (Wyco NT1100, Veeco, Woodbury, NY). Figure 4 shows the 3D measurement of the gold sample, while Figure 5 shows its surface height distribution. The root mean square (rms) height for this sample was about $6.6 \mu\text{m}$.

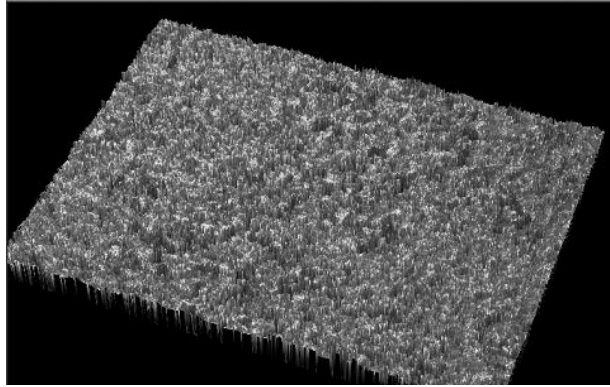


Figure 4– 3 D image of gold coated rough surface sample

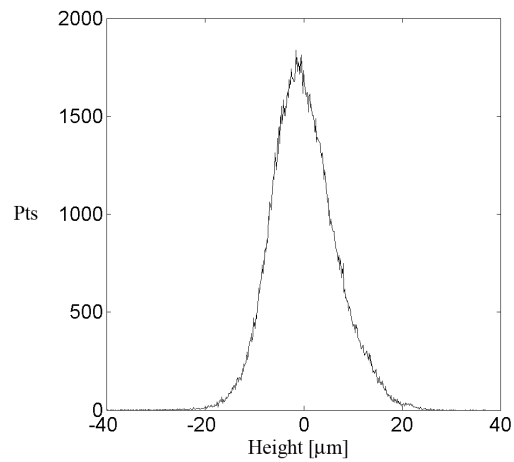


Figure 5 – Height distribution of gold coated rough surface sample

The interferometric microscope is unable to accurately measure highly scattering samples. For this reason, the witness skin samples were coated with gold before performing surface height measurement. Results are shown in Figs. 6 and 7. The rms height for these skin samples was about 23 μm.

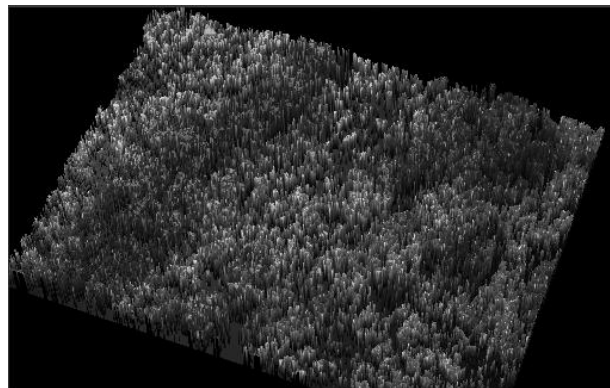


Figure 6 – 3 D image of gold coated skin sample

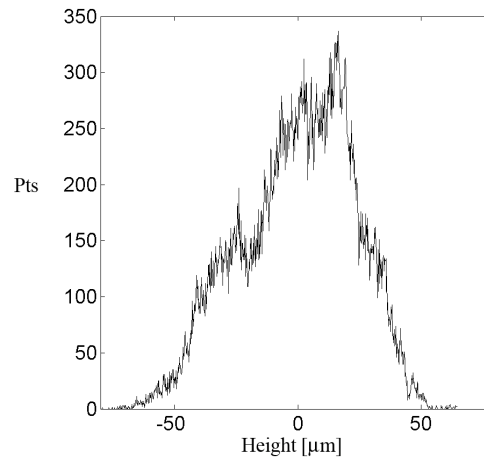


Figure 7 – Height distribution of gold coated skin sample

All experiments were conducted first with the bare sample, in order to measure the light backscattered by the rough surface, then the sample was smeared with a moisturizing transparent gel and covered with a round 0.25 mm thick piece of glass. By matching the air-tissue boundary with the glass, we generated a flat surface for the incident light.

3. RESULTS

3.1 In-plane measurements

For every source angle, two images were captured: one with co-polarized optics (*pp*) and one with cross-polarized optics (*ps*). The value *Pol* was calculated from Eq. 1. Figure 8 shows some *Pol* images for the 543 nm light. The top row shows images for three different source incident angles taken with the matched boundary, while the bottom layer corresponds to the unmatched (rough) boundary. The round glass cover slip is visible on the top row. The images on the top row are darker (corresponding to lower *Pol* values) compared to the bottom row images, due to the fact that some of the light specularly reflected from the rough surface was eliminated by matching the boundary.

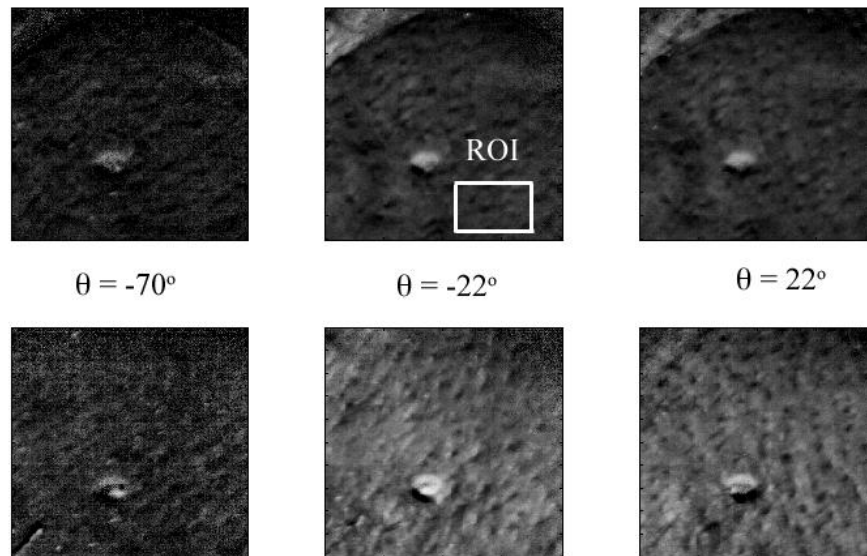


Figure 8 – Measured *Pol* images for matched boundary (top row) and unmatched boundary (bottom row) for a porcine skin sample for three different incident angles. The source wavelength was 543 nm. The source wavelength was 543 nm. The size of the image is approximately 17×17 mm². Measured normal to the surface with the source inclined of an angle $\theta = -70^\circ$, -22° , and 22° respectively.

A region of interest (ROI) of 20×30 pixels, shown in Fig. 8, was collected in every image and the mean of the *Pol* was calculated. Results for the matched and unmatched boundaries are shown in Figs. 9 and 10, respectively, for all three wavelengths. The value *Pol* is an indicator of the degree of linear polarization of the image.

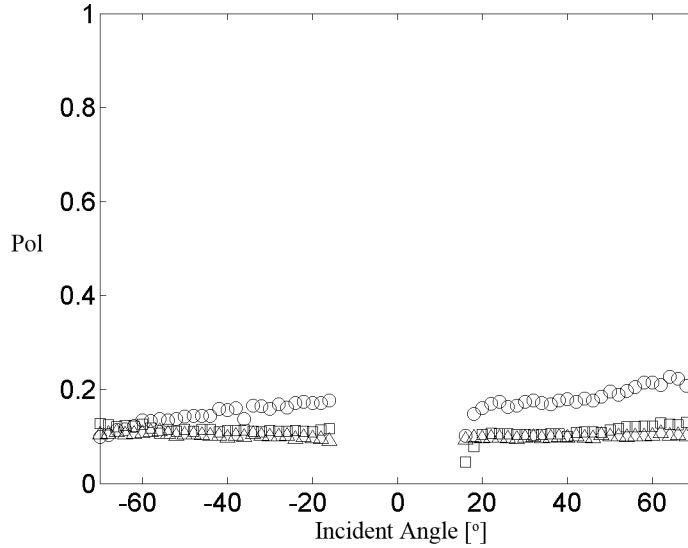


Figure 9 – Mean value of *Pol* for a 20×30 pixel region of interest for the skin sample with a matched boundary for 543 nm (circles), 633 nm (squares), and 689 nm (triangles). Measured normal to the surface, varying the angle of illumination θ .

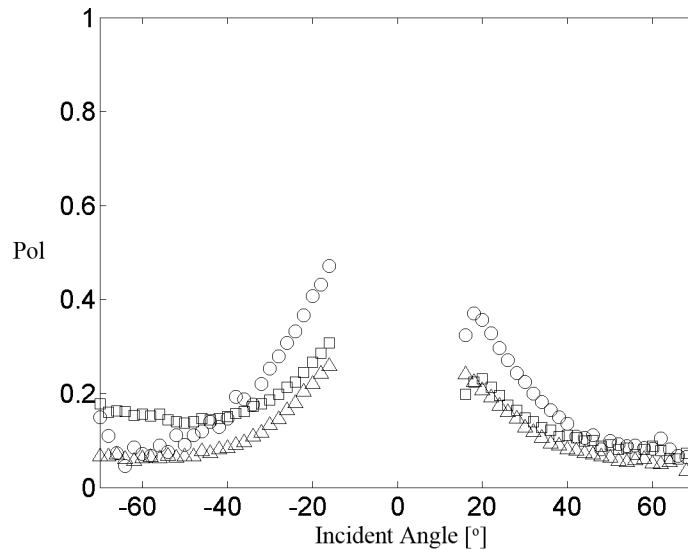


Figure 10 – Mean value of *Pol* for a 20×30 pixel region of interest for the skin sample with an unmatched boundary for 543 nm (circles), 633 nm (squares), and 689 nm (triangles). Measured normal to the surface, varying the angle of illumination θ .

The results obtained with the matched and unmatched boundaries are very different. Not only is *Pol* lower for the matched boundary, but it is also constant for all of the measured angles. For the unmatched surface, the tails of a broad reflection peak is visible around 0°. While results are unavailable for $-15^\circ < \theta < 15^\circ$, due to obscuration of the incident beam by the camera, the general trend is nevertheless clearly visible. These images suggest that the rough surface strongly contributes to the *Pol* image when the

boundary is unmatched. Both surface and subsurface reflections contribute to the total image and are indistinguishable. The observed wavelength dependence is due to the wavelength dependence of the scattering coefficient⁴. This effect has been explored elsewhere⁵.

Figures 11 and 12 show results when the region of interest is on top of a pigmented nevus. The matched boundary image results do not vary strongly for different incident angles. The slight off-specular peak visible in Fig. 11 can be attributed to the non-flat surface of the nevus.

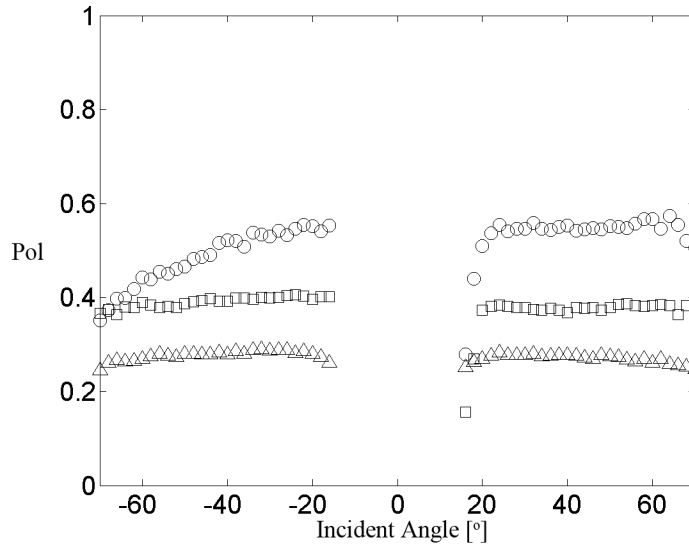


Figure 11 – Mean value of Pol for a 20×30 pixel region of interest containing a nevus with a matched boundary for 543 nm (circles), 633 nm (squares), and 689 nm (triangles). Measured normal to the surface, varying the angle of illumination θ .

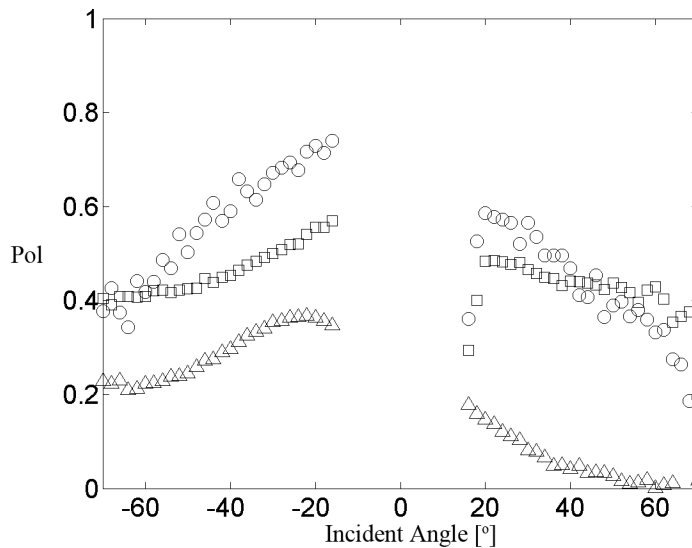


Figure 12 – Mean value of Pol for a 20×30 pixel region of interest containing a nevus with an unmatched boundary for 543 nm (circles), 633 nm (squares), and 689 nm (triangles). Measured normal to the surface, varying the angle of illumination θ .

3.2 Out-of-plane measurements

Out-of-plane measurements were conducted at 543 nm. Figure 13 shows some of the results, the top row corresponding to a matched boundary condition and the bottom row to a rough, unmatched boundary. Images were taken for different azimuth angle ϕ maintaining a fixed inclination angle θ .

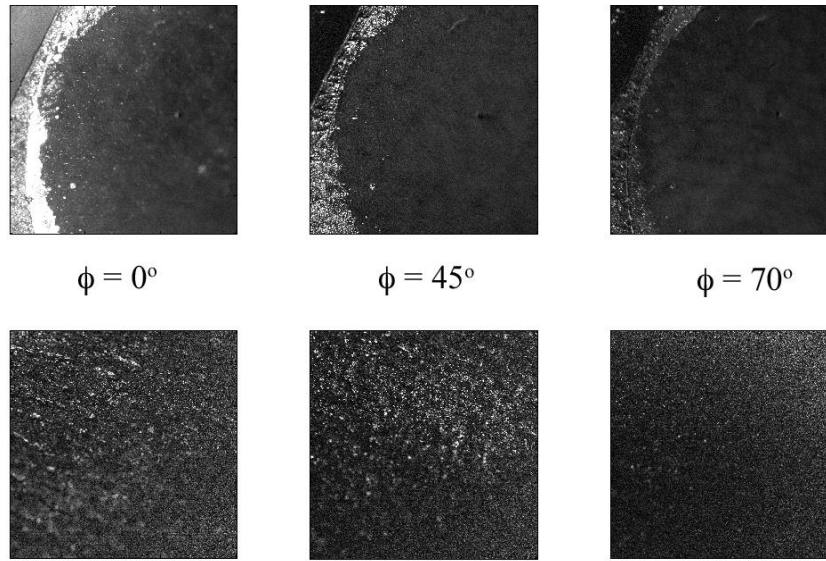


Figure 13 – *Pol* images for matched boundary (top row) and unmatched boundary (bottom row) for a porcine skin sample measured in the out-of-plane configuration for three different azimuthal incident angles. The source wavelength was 543 nm. The size of the image is approximately 17×17 mm². Measured at an angle $\theta = 45^\circ$ with the illumination at an angle $\theta = 45^\circ$ and $\phi = 0^\circ, 45^\circ$, and 70° respectively.

Two different materials were studied in the out-of-plane configuration, a rough gold sample and porcine skin samples. Figure 14 shows the mean and standard deviation of *pp* and *ps* within a region of interest for the gold sample as a function of the azimuth angle ϕ . The raw *pp* and *ps* images were normalized by their sum ($pp + ps$). A facet scattering model from the SCATMECH/MIST library⁶ was used to model the data (using optical constants for gold at 543 nm: $n = 0.39$ and $k = 2.59$).

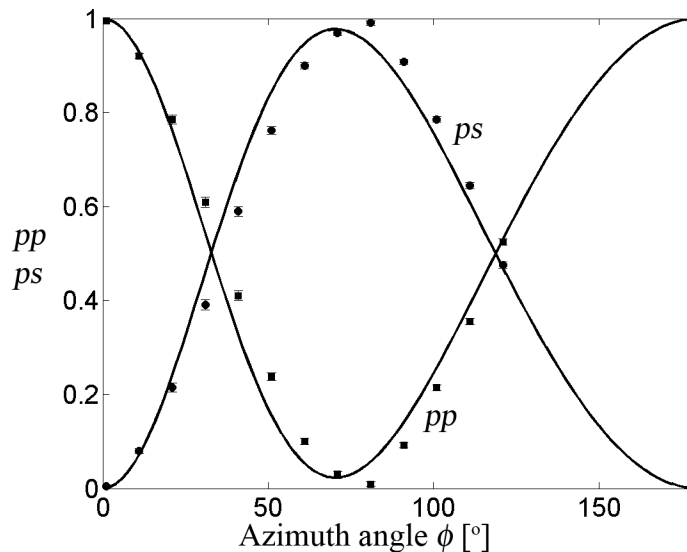


Figure 14 – The normalized mean value of *pp* and *ps* for a rough surface gold sample. The error bars represent twice the estimated standard deviation of the mean, and represent the Type A (statistical) 95 % confidence level uncertainties. The curves show the predictions of a facet scattering model. Measured at an angle $\theta = 45^\circ$, varying the illumination azimuth angle ϕ , holding the illumination polar angle $\theta = 45^\circ$.

Another metric for characterizing the scattered light is the orientation angle of the polarization ellipse, η ,

$$\eta = \frac{1}{2} \text{atan} \left(\frac{S_2}{S_1} \right) \quad (2)$$

where S_1 and S_2 are the second and third elements of the Stokes vector, given by

$$\begin{aligned} S_1 &= 2ps - 2pp \\ S_2 &= 4p45 - 2ps - 2pp \end{aligned} \quad (3)$$

Germer showed⁷ that the behavior of η can be very sensitive to the scattering mechanism, and is insensitive to the unpolarized fraction of the light. Figure 15 shows the results for η , along with the predictions of facet scattering model.

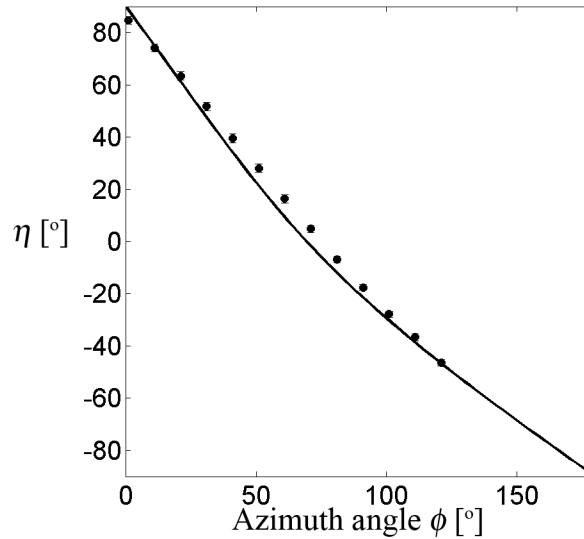


Figure 15 – Mean polarization angle η measured from the rough gold sample. The error bars represent twice the estimated standard deviation of the mean, and represent the Type A (statistical) 95 % confidence level uncertainties. The curve represents the prediction of a facet scattering model. Measured at an angle $\theta = 45^\circ$, varying the illumination azimuth angle ϕ , holding the illumination polar angle $\theta = 45^\circ$.

Figures 16 and 17 show the behavior of rough unmatched (full symbols) and matched (open symbols) porcine skin samples. The behavior of pp and ps for the two different samples differs only for $\phi < 50^\circ$. This is an important finding showing that non-contact measurements can be done when the azimuth and inclination angles are chosen appropriately, e.g., for $\phi > 50^\circ$ and $\theta = 45^\circ$.

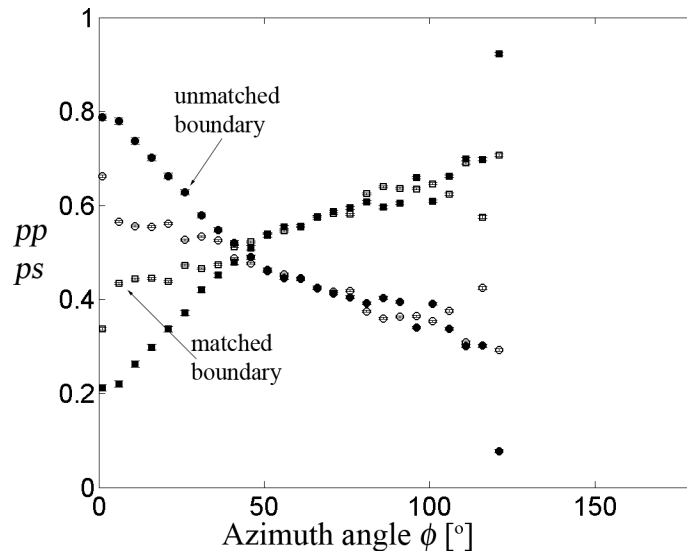


Figure 16 – The normalized mean value of pp (circles) and ps (squares) for the porcine skin sample. The error bars represent twice the estimated standard deviation of the mean, and represent the Type A (statistical) 95 % confidence level uncertainties. Measured at an angle $\theta = 45^\circ$, varying the illumination azimuth angle ϕ , holding the illumination polar angle $\theta = 45^\circ$.

Figure 17 shows interesting behavior for the polarization angle η . The curve shows the results for the facet model using an index of refraction appropriate for the skin ($n = 1.4$). The unmatched boundary sample tends towards the facet scattering model, although not perfectly. The matched boundary sample deviates away from this model significantly, tending upwards towards 90° or downward towards -90° . These results are consistent with a model for diffuse scattering under a flat interface.

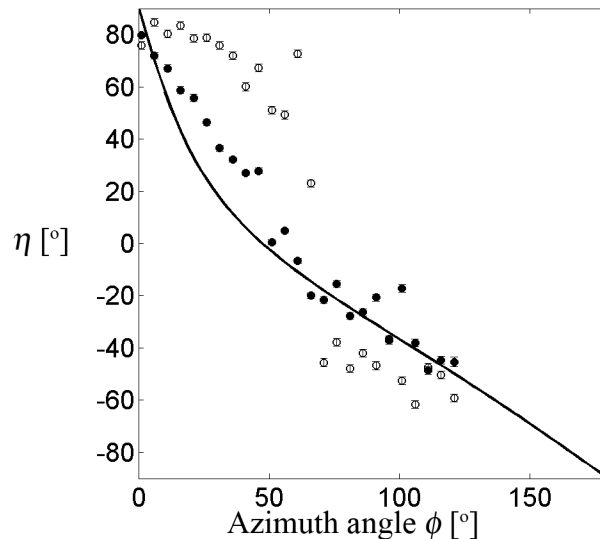


Figure 17 – Mean polarization angle η measured from the porcine skin sample. The error bars represent twice the estimated standard deviation of the mean, and represent the Type A (statistical) 95 % confidence level uncertainties. The curve represents the prediction of a facet scattering model. Measured at an angle $\theta = 45^\circ$, varying the illumination azimuth angle ϕ , holding the illumination polar angle $\theta = 45^\circ$.

By choosing θ and ϕ appropriately, we can remove both surface and multiple diffuse scattering. Figures 18 and 19 show an example of this effect. Two images of the porcine skin were obtained under

two different illumination conditions and viewing polarizations. For both images, the illumination is *p*-polarized. However, for one the illumination is from $\phi = 70^\circ$ and the camera is viewing *p*-polarized light, while for the other the illumination is from $\phi = 0^\circ$ (the specular direction) and the camera is viewing *s*-polarized light (crossed polarization). In both cases, there was no glass cover slip, and the specular reflection is effectively removed, one geometrically, and one polarimetrically. Since the sample and the camera do not move, the registry between the images does not change. Combining the two images we can calculate the “effective” *Pol* image shown in Fig. 19. This derived image shows features which are distinctly subsurface, eliminating both surface and multiply scattered light.

4. CONCLUSION

We demonstrate new methods for using polarized light imaging to highlight subsurface features. The measurements rely upon out-of-plane polarized illumination with polarization-sensitive viewing. The scattering by rough skin and gold shows behavior which is reasonably well described by a facet scattering model. The diffusely scattered light shows behavior which is essentially unpolarized. By combining images with different illumination and viewing configurations, an image can be produced which shows significant subsurface structure.

5. REFERENCES

1. R.R. Anderson, “Polarized light examination and photography of the skin.” *Arch. Dermatol.* **127**, 1000-1005, (1991)
2. L. Jacques, J. C. Ramella-Roman, K. Lee. “Imaging skin pathology with polarized light,” *J. Biomed. Optics*, **7**, 329-340, (2002).
3. T. A. Germer and C. C. Asmail, “Polarization of light scattered by microrough surfaces and subsurface defects”, *J. Opt. Soc. Am. A*, **16**, 1326-1332 (1999).
4. S. Saidi, S. L. Jacques, F. K. Tittel, “Mie and Rayleigh modeling of visible-light scattering in neonatal skin,” *Applied Optics* **34**, 7410-7418, (1995).
5. J.C. Ramella-Roman, and S.L. Jacques, “Mueller matrix description of collimated light transmission through liver, muscle and skin,” *Laser-Tissue Interaction XII: Photochemical, Photothermal, and Photomechanical*, *Proc. SPIE*, **4257**, 110–116. 2001.
6. T. A. Germer, *SCATMECH: Polarized Light Scattering C++ Class Library* available from <http://physics.nist.gov/scatmech>.
7. T. A. Germer, “Angular dependence and polarization of out-of-plane optical scattering from particulate contamination, subsurface defects, and surface microroughness”, *Appl. Opt.* **36**, 8798-8805 (1997).
8. Certain commercial equipment, instruments, or materials are identified in this paper in order to specify the experimental procedure adequately. Such identification is not intended to imply recommendation or endorsement by the National Institute of Standards and Technology or Johns Hopkins University, nor is it intended to imply that the materials or equipment identified are necessarily the best available for the purpose.

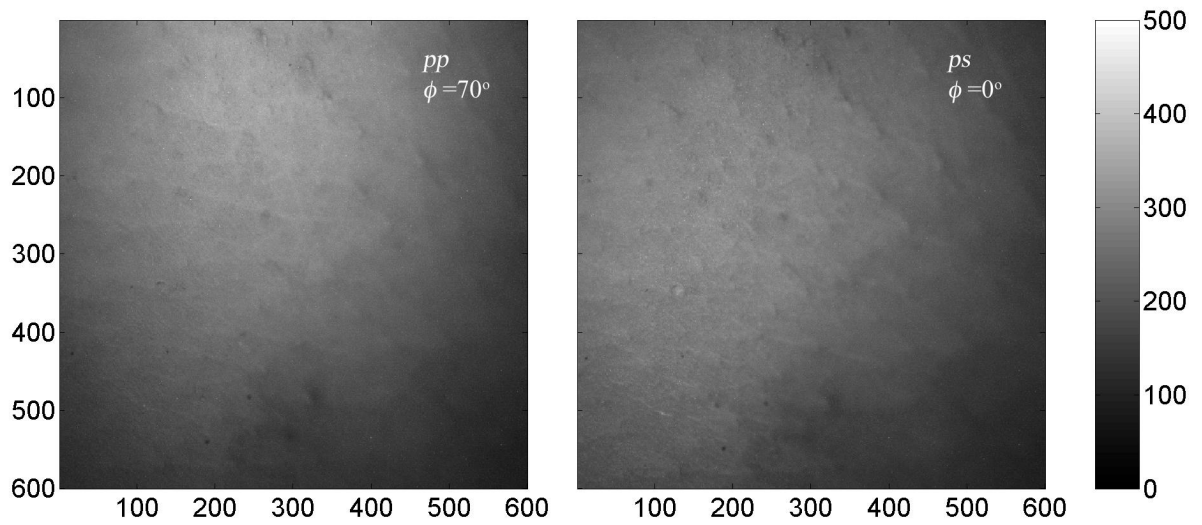


Figure 18 – Images measured in (left) the pp configuration and $\phi = 70^\circ$ and (right) the ps configuration and $\phi = 0^\circ$. The source wavelength was 543 nm. The size of the image is approximately $24 \times 24 \text{ mm}^2$.

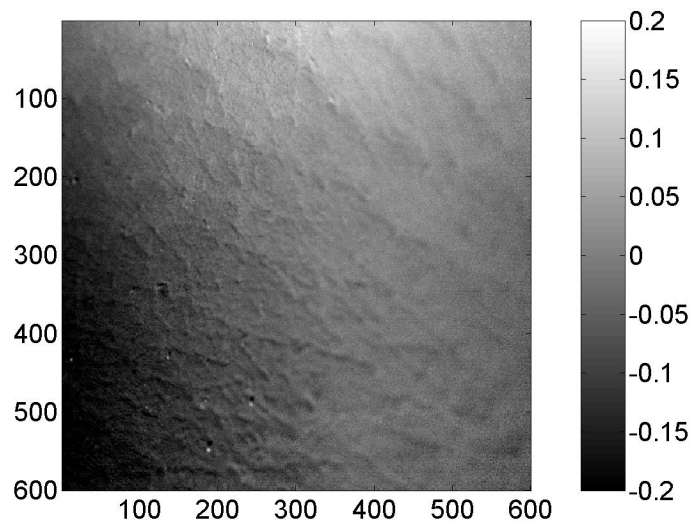


Figure 19 – Derived effective Pol image using the data in Fig. 18, using $pp(\phi = 70^\circ)$ and $ps(\phi = 0^\circ)$. The size of the image is approximately $24 \times 24 \text{ mm}^2$.